

Specificity and Synergy at the Oil–Brine Interface: New Insights from Experiments and Molecular Dynamics Simulations

Safwat Abdel-Azeim,* Sivabalan Sakthivel, Tarek A. Kandiel, and Mazen Y. Kanj



Cite This: *Energy Fuels* 2021, 35, 14647–14657



Read Online

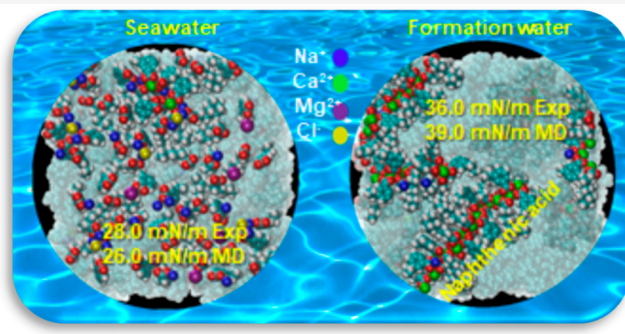
ACCESS |

Metrics & More

Article Recommendations

Supporting Information

ABSTRACT: The interfacial tension (IFT) between oil and brine is a key parameter affecting the enhanced oil recovery process. Despite the several theoretical and experimental investigations on the oil–brine system, the salinity effect on the IFT of oil–brine is still not fully understood. There is a contradiction in the literature rather than consistency. In the present study, we combine molecular dynamics (MD) simulations with the pendant drop method to investigate the molecular interactions at the oil–brine interface to better understand the salinity–IFT relationship. Herein, we are taking into account the complex composition of both crude oil and brine and the pH and total acid number. Different salinity conditions have been considered ranging from deionized water to connate (formation) water. We also consider the effects of individual brines of the main alkali salts (i.e., NaCl, MgCl₂, and CaCl₂) that are common in carbonate reservoirs. The specificity and synergy of the molecular interactions are observed via the confrontation of the results of the mixed brines (seawater and formation water) with those of the individual brines. We observed a significant impact of the divalent cations on the oil–brine interfacial tension. Due to the specificity of the organic acid–Ca²⁺ type of interaction and the synergy between the different ions, complete encapsulation of the Ca²⁺ ions has been observed within the formation water brine. This induces the depletion of the organic acids at the interface and thus increases the IFT. Such ionic encapsulation has not been observed in the individual brines because the cation–anion (Cl[−]) and the cation–water interactions are strong enough to prevent the cation–acid encapsulation. The interplay between the electrostatic interactions and the cations' dehydration-free energies is the main parameter that controls their specificity and synergy, affecting the oil–brine interfacial properties. This work provides important details on the ionic interactions influencing the interfacial properties between crude hydrocarbons and brine.



1. INTRODUCTION

Oil–water interfaces are common with many implications in nature and industrial applications such as environmental cleaning and the oil industry. It is well-established that interfacial tension (IFT) is a critical factor in the oil recovery process. It affects the capillary forces through which the trapped oil could be mobilized.^{1–3} Understanding IFT and its controlling factors such as temperature, pressure, salinity, total acid number, base number, and pH are paramount to exploring more oil using unconventional methods.^{4–6} On the one hand, crude oil has a complex composition with four components: alkanes, aromatic, asphaltene, and resin.^{7,8} Each of these components has a complex structure. For example, asphaltene has many proposed structural models due to the lack of rigorous experimental data. On the other hand, the brine composition is complex and variant. The salinity in the Saudi Arabian reservoirs varies from seawater at about 7 wt % of total dissolved solids (TDS) to the formation (connate) water at nearly 25 wt % TDS. Understanding the oil–water flow in porous media is critical for improving the efficiency of the tertiary oil recovery method. It is known that primary and

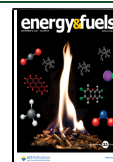
secondary recovery methods could only extract 30–50% of the oil retained underground.^{9–11} Chemical enhanced-oil-recovery (cEOR) is widely considered and applied as a tertiary recovery method, particularly in field pilots.^{12–15} One of the essential components of cEOR formulations is surfactants, in addition to polymers. Surfactants are used to reduce the oil–water IFT as an efficient way to reduce the residual oil saturation.^{16–18} One of the crucial phenomena that control the oil–water flow is the interfacial tension. Bringing the IFT of the oil–water system into the ultralow regime (10–2–10–3 mN/m) is desirable for better recovery.^{19–21}

Many experimental and theoretical investigations have been reported so far on the oil–deionized water IFT, focusing on

Received: June 29, 2021

Revised: August 18, 2021

Published: August 30, 2021



the temperature and pressure effects.^{22–30} The salinity effect on brine–oil IFT remains in debate, and there is a contradiction in the literature rather than consistency. One group of researchers observed a negative impact of salinity on IFT.^{20,31,32} A second group observed a complex trend.^{33–36} They detected first a decrease followed by an increase in the IFT as salinity increases and IF reincreases again as the salinity further increases. The third group found a negligible impact of salinity on the IFT.^{37–39} The most reported studies do not consider the brine's complex composition and substitute it with simple NaCl solutions.^{40,41} Li et al., in a recent study, considered N-, S-, and O-bearing polar components in their oil model to represent the oil complexity, but they ignored both pH and brine composition.⁴⁰ Experimentally, the complex brine composition plays an important role and significantly impacts the oil recovery at the reservoir temperature.⁴² Furthermore, most studies in the literature use a simple hydrocarbon to represent the crude oil phase (e.g., octane, decane, or dodecane) and ignore the crude oil's structural complexity.^{8,43} The many controversies in the literature on IFT trends might be due to the crude oil and brine composition's diversity.⁴⁴ Some researchers did not consider the polar components in modeling the oil despite its essential impact on the IFT.^{44,45}

Salting-in and salting-out are the two most favorable mechanisms for explaining the salinity effect on IFT. At low salinity, salting-in accelerates the diffusion of the surface-active molecules from the bulk of the oil into the interface, resulting in reduction of the IFT. The oil phase's polar components favor the oil phase at high salinity, and the salting-out is the dominant effect. The presence of cations in the aqueous phase alters the interface and breaks down the hydrogen bonds between the oil polar components and water, leading to an increase in the IFT.^{46–48} As mentioned above, there is no clear understanding of the IFT–salinity relationship. There is more controversy than clarity in the literature in this regard, and the specific ionic effect on IFT is poorly reported. Lashkarbolooki et al. investigated the impact of different brine types (NaCl, KCl, Na₂SO₄, MgSO₄, CaSO₄, CaCl₂, and MgCl₂) on the oil–water IFT with a focus on low brine concentrations and acidic crude oil with a TAN of 1.6 mg KOH/g, which is not relevant for more acidic oil.⁴⁹ More recently, Kirch et al.⁵⁰ have assessed a machine learning model against MD simulations on the oil–brine IFT. Though they used different crude oil compositions, they neglect resin, asphaltene, pH, and the naphthenic acids in their model.

This study combines atomistic MD simulations with the pendant drop method to investigate the specificity and synergy of the molecular interactions in order to understand the effect of salinity on IFT. We considered the complex composition of both brine and crude oil. We examine the effect of both mono- and divalent cations that commonly exist in the Saudi Arabian carbonate reservoirs. A more realistic crude oil model has been built based on the Saturate, Aromatic, Resin, and Asphaltene (SARA) composition of the crude oil and its TAN analysis. The model was validated against experimental IFT of the oil–deionized water. Our study aims to achieve more profound and atomic level details of the molecular interactions at the oil–brine interface. Such a deep understanding would help to optimize cEOR formulations that target IFT reduction and wettability alteration.

2. METHODOLOGY

2.1. Experimental Measurements. 2.1.1. Interfacial Tension Measurement.

The pendant drop method is used to measure the interfacial tension between the Arabian crude oil and brine solutions using a Tensiometer (IFT-700 from Vinci Tech). The setup contains an aqueous phase sample holder, a high-pressure/high-temperature cell, a syringe of oil (protruding from the bottom of the cell), accumulators for fluids storage, and hydraulic pumps. A high-resolution camera is used to capture the images, and user interface software is used to analyze the drop shape and diameter. The oil droplet is generated in the aqueous phase from the bottom of the cell. The static drop is stabilized when it is of maximum size (just before it detaches) and then photographed and the drop dimensions measured using the built-in software.^{51–53}

2.1.2. Total Acid Number. The ASTM 974 standard test method^{54,55} was used to measure the quantity of the acidic components that are present in the crude oil by facile acid–base neutralization titration. In a typical titration, 0.2 g of the oil sample is dissolved in a mixture of toluene and isopropyl alcohol. The mixture (a yellow-orange coloration) is titrated against a standard KOH dissolved in isopropyl alcohol (0.1 M). The end point is indicated using p-naphtholbenzene. TAN is calculated using eq 1 and reported as mg KOH/g of crude oil (see Table 1).

$$\tan = \left[\frac{VN \times 56.10}{WT} \right] \quad (1)$$

where V is the volume of KOH (mL), N is the concentration of KOH (mmol/mL), and WT is the amount of oil in gram.

Table 1. Ionic Concentrations in ppm for the Three Mixed Brines Used in This Work⁷⁴

ions	SW	50%_FW	FW
Na ⁺	18 300	29 745	59 491
Ca ²⁺	650	9,520	19 040
Mg ²⁺	2110	1220	2439
SO ₄ ²⁻	4290	175	350
Cl ⁻	32 200	66 030	132 060
HCO ₃ ⁻	120	177	354
TDS	57 670	106 867	213 734

2.1.3. SARA Composition Analysis. The Modified ASTM D3279 and D2007^{56,57} were used to quantify the crude oil's SARA composition. In a typical test, 10 g of the oil sample is taken in a beaker and deasphalting using *n*-heptane. The remaining residual maltenes compounds (saturates, aromatics, and resins) are isolated using a glass chromatography column with activated silica as the adsorbent. The saturated compounds are eluted out first using *n*-heptane as eluting solvents (about 100 mL); sequentially, aromatics were eluted using toluene as a solvent (100 mL). The remaining resin is eluted with toluene–methanol (50:50), methanol–chloroform (50:50), chloroform, and acetonitrile solvents. Results are provided in Table S1.

2.2. Computational Details. All MD simulations were conducted using the GROMACS 5.4.1 code⁵⁸ and OPLS-AA^{59,60} plus SPCE⁶¹ force fields, which successfully described this kind of system in previous reports.^{62–65} Systems were first energy minimized with the steepest descent method to a convergence on the maximum force of 100 kJ/(mol nm). The

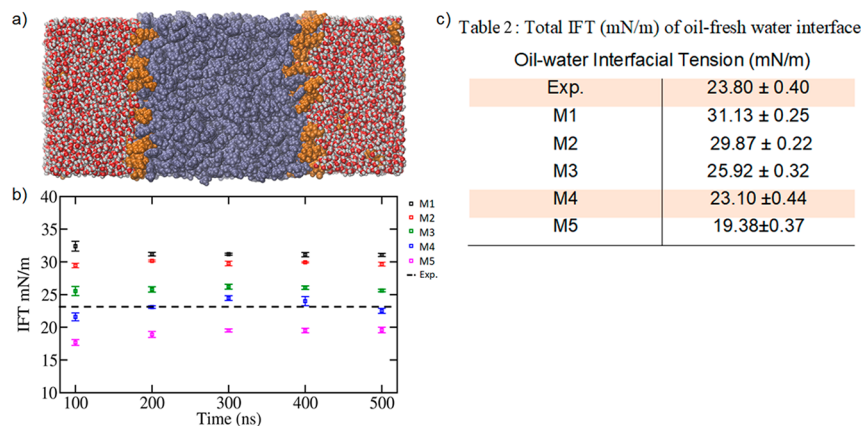


Figure 1. (a) Oil–water interface (oil model is M4). Oil is shown in ice-blue spheres; the organic acids are shown in orange spheres. Waters are shown in red and white spheres. (b) IFT as a function of time using different oil models. The dashed line is the experimental IFT. The block average of IFT over 200–500 ns is reported in Table 2 (c), with the experimental IFT average over three replicates.

particle-mesh Ewald (PME) algorithm⁶⁶ was applied to treat the electrostatic interactions with a cutoff of 1.2 nm for van der Waals (VDW) and short-range electrostatic interactions. All bonds involving hydrogen atoms were constrained by the LINCS algorithm.⁶⁷ The system was coupled to a thermal bath using a Nose–Hoover thermostat^{68,69} with a time constant of 0.1 ps for equilibration and 0.5 ps for production. The pressure was controlled with Parrinello–Rahman barostat⁷⁰ with a time constant of 2 and 5 ps for equilibration and production, respectively. The system’s thermalization at the required temperature has been done in the constant number of particles, volume, and temperature (NVT) thermodynamic ensemble. The equilibration is performed in the constant number of particles, volume, and pressure (NPT) ensemble. Interfacial tension simulations are carried out in the NP_nAT ensemble, P_n and A are the normal pressure perpendicular to the interface (i.e., the z direction) and the interfacial area in the xy plane, respectively. A time step of 2 fs was set for the simulations, and the coordinates were saved at 10 ps intervals. Trajectories are analyzed using GROMACS tools.

2.2.1. The Model of the Brine–Oil Interface. In order to have mechanistic insights on the IFT changes upon the ionic composition alteration of the injected brines, we built a multicomponent structural model based on SARA and TAN values determined experimentally (Table S1 and Figure S1). Our heavy crude oil is based on a mixture of light oil from Kunieda et al.⁷¹ and an oil model from Sedghi et al. (Figure S1).⁴⁴ Asphaltene and resin structure models are adopted from Jien et al.⁷² and Mikami et al.,⁷³ respectively. MD simulations are performed for a long time (500 ns) to ensure convergence and decrease IFT uncertainty. A large enough interfacial area (36 nm²) was used to simulate the oil–brine system with a simulation box of 6 × 6 × 13.5 nm³ (Figure 1a). In MD simulations, we considered deionized water, seawater (SW), 50% diluted formation water (FW_50%), and full salinity formation water (FW). We added different organic acids (ethylbenzoic, nonanoic, and 3-cyclohexyl propanoic acid) to reflect the TAN of the crude oil. SARA ratios are considered when the relative ratio of these acids is determined. For example, we added 50% of these acids as ethylbenzoic because crude oil has a high percentage of aromatics. We have generated six models for the crude oil; model M1 is a mixture of 13 hydrocarbons: hexane, heptane, octane, nonane, cyclohexane, cycloheptane, toluene, benzene, asphaltene,

resin, ethylbenzoic, nonanoic, and 3-cyclohexyl propanoic acid with 64, 70, 69, 58, 43, 26, 150, 478, 1, 3, 44, 22, and 66 molecules, respectively. The organic acids in this model are in the protonated state, while in M2, we considered 50% of the organic acids in their deprotonated state. All the organic acids are built in their deprotonated state in M3 and distributed randomly in the oil phase. In M4, we considered them aligned in a monolayer structure at the oil–water interface, and they all are deprotonated. We have incrementally increased the organic acid composition by 50% more in M5 (i.e., 66, 34, and 100 molecules for the ethylbenzoic, nonanoic, and 3-cyclohexyl propanoic acid, respectively, divided over the two oil–brine interfaces), and 100% more in M6 (i.e., 88, 44, 132 molecules for the ethylbenzoic, nonanoic, and 3-cyclohexyl propanoic acid, respectively, divided over the two interfaces). The ionic compositions of seawater and formation brines are taken from previous work (Table 1).^{62,74} In addition to seawater and formation water salinity, we considered the individual brines (i.e., NaCl, CaCl₂, and MgCl₂). Four concentrations were considered for each cation (Na⁺, Ca²⁺, and Mg²⁺) and ranged from 1 to 5 M. Experimentally, the concentration range varied from 0.01 mM to 5 M with 10 concentration values for each brine. Concerning NaCl parameters, Åqvist’s parameters are adopted for Na⁺⁷⁵ and OPLS for Cl⁻.⁷⁶ IFT calculations are carried out using the Kirkwood–Buff equation (eq 2).

$$\gamma = \frac{Lz}{2} \left| \langle P_{zz} \rangle - \frac{1}{2} (\langle P_{xx} \rangle + \langle P_{yy} \rangle) \right| \quad (2)$$

where Lz is the average length of the simulation box in the z-axis direction; P_{zz}, P_{xx}, and P_{yy} are the diagonal pressure tensors averaged over time and positions. Further analyses are carried out using Gromacs analysis tools.

3. RESULTS AND DISCUSSION

MD simulations are combined with the pendant-drop experiments for in-depth investigations of the brine–oil interfacial properties. More recent studies considered the salinity effect on IFT of oil–water using polar components such as S-, N-, and O-bearing molecules. They confirmed a strong impact of O-bearing components on IFT reduction.⁴⁰ Also, Kirch et al.⁵⁰ have assessed the application of a machine learning tool coupled with MD for fast IFT estimation. Despite the previous rigorous approaches to examine the IFT of brine–oil systems, these studies did not consider the effect of pH,

salinity variations (at high concentrations), the SARA of natural oil, or the TAN value. Therefore, in this study, we consider all the parameters mentioned above that could affect the oil–brine interfacial properties. The aim is to gain atomistic insights into the salinity–IFT relationship.

3.1. Approach Validation. We have already benchmarked the OPLS-AA force field using the density and IFT of different hydrocarbons used in the light crude oil model.⁶² In this work, MD simulations predicted the Arabian crude oil density at 842 kg/m³ with an estimated error of less than 4%. This further supports the validity of using OPLS-AA and our model to represent the Arabian crude oil. The calculated IFT for the oil–fresh water compares well against a measured value of 23.80 ± 0.40 mN/m and is in good agreement with the reported IFT of the Iranian crude oil,⁴⁹ which is similar to our oil. To represent the high acidity of the Arabian crude oil (TAN = 6.5 mg KOH/g oil),^{77,78} we generated five models (M1–M5) for the oil–fresh water interfaces as detailed in the *Methodology* section. Figure 1b indicates that IFT converges in most cases within 300 ns or less. All simulation runs were extended to 500 ns to ensure complete convergence. To get better statistics, we used the block averages of IFT with an interval of 100 ns (i.e., take the average and standard deviation every 100 ns) and took the final IFT as the average of the interval averages started from 200 ns (Figure 1c).

Similarly, the final standard deviation is the average of the interval's standard deviations. The best match of the calculated IFT with the experimental counterpart is model M4 (MD, 23.10 ± 0.44 mN/m; Exp, 23.80 ± 0.40 mN/m), in which the organic acids are deprotonated and display a monolayer structure. As the organic acids accumulate and arrange in a monolayer structure at the interface, IFT is reduced (see the trend from M1 to M4). The IFT reduction is induced by the diffusion and alignment of the organic acids at the interface. The organic acids interact strongly with water molecules; especially, we have a crude oil of low viscosity (15.37 cP) that easily permits their diffusion. When we further increased the organic acid concentration at the interface (M5), IFT was further reduced (Table 2 of Figure 1).

The 2D density map of the organic acids shown in Figure S2 indicates the organic acids' alignment at the interface in M4 and the disorder arrangement in M3. The monolayer alignment of the organic acids at the interface enhances the molecular interactions between the oil and water phases, which causes a reduction of IFT by 2.4 mN/m. To examine the organic acid stability at the interface in the two models (i.e., M3 and M4), we have calculated their interaction energies (electrostatic and Van Der Waals contributions) with the two phases. The interaction energy is normalized by the total number of organic acids in the system. In M4, organic acids establish stronger interactions with the aqueous phase by -4.0 kJ/mol lower than in M3. At the same time, weak nonpolar interactions are observed with the oil phase in both models (the energy difference is only -0.5 kJ/mol). The partial density of the main components in the two phases at the interface showed that the concentration of the organic acids at the interface in M4 is slightly higher than in M3 (Figure S3). It seems that the potential energy surface is very flat and can sample many different conformations within a small window of energy. It is worth mentioning that the considered organic acids do not have a long hydrophobic tail. The area per molecule in M4 is 0.49 nm, close to that of sodium dodecyl sulfate (SDS). Nevertheless, the organic acids are not as

efficient as SDS for the IFT reduction. This is due to the weaker interaction of the organic acids with the oil phase caused by their short tail compared to SDS. Altogether, the agreement between the MD and the experimental IFT validates and supports our model and the force field parameters to investigate the Arabian crude oil–brine interfacial properties.

3.2. Effect of Salinity on the Oil–Brine IFT (Mixed Brines).

We have investigated the oil–brine interfaces, including seawater, 50% diluted formation water, and full salinity formation water. Figure 2 and Table S2 indicate that

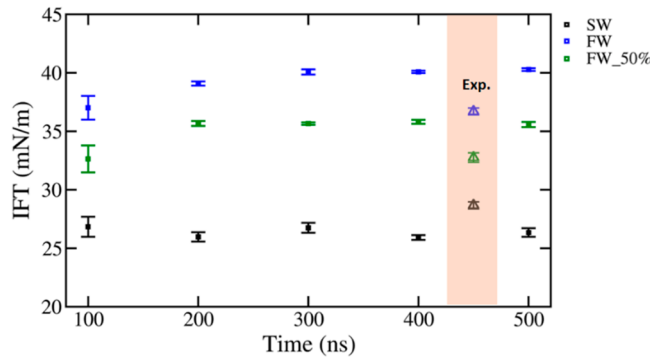


Figure 2. IFT of seawater, formation water, and 50% diluted formation water as a function of time calculated using the oil model M4.

salinity has a negative impact on the IFT of the oil–brine solutions. The IFT increases along with the salinity. These results agree well with what is reported for the Iranian oil from the carbonate reservoir, which is similar to our crude oil.²⁰ There is a good agreement between the experimental and the calculated IFT using M4. The organic acids are aligned in a monolayer adsorbed at the oil–brine interface (at their deprotonated states). The cations in brine solutions stabilize the carboxylate anions of the organic acids via strong electrostatic interactions and form different chelating structures (Figure 3). The pK_a of these organic acids (around 4.5)⁷⁹ supports their deprotonated forms at a pH higher than 7.0. The injected fluids for EOR applications in carbonate reservoirs are usually alkaline with a pH of around 10.0.⁸⁰ The petroleum surfactant (organic acids in crude oil) is usually generated by adding alkaline additives such as Na_2CO_3 or ammonia to the cEOR formulations.

We have to emphasize that the objective here is not to reproduce the exact experimental IFT values but to observe the general salinity–IFT trend. To do so, we have tuned the amount of the deprotonated organic acids at the interface. To minimize the computational cost, we limited the simulations to models M4 (Figure 2 and Table S2) and M5 (Figure S4 and Table S3). As reported in the literature, the salinity effect on the oil–brine IFT can be explained by the salting-in and out effects (Figure S5). At low salinity brines, the salting-in is the dominant factor, which leads to the solubility of organic acids from the oil phase to the aqueous phase. The texture of the interface depends on the brine's salinity; in SW, the organic acids cover almost the entire interface. As the brine's salinity increases, the organic acids are getting concentrated and cover a limited area of the oil–brine interface. The presence of the divalent cations (Ca^{2+}) that have the ability to form multidentate structures with the organic acids is the main

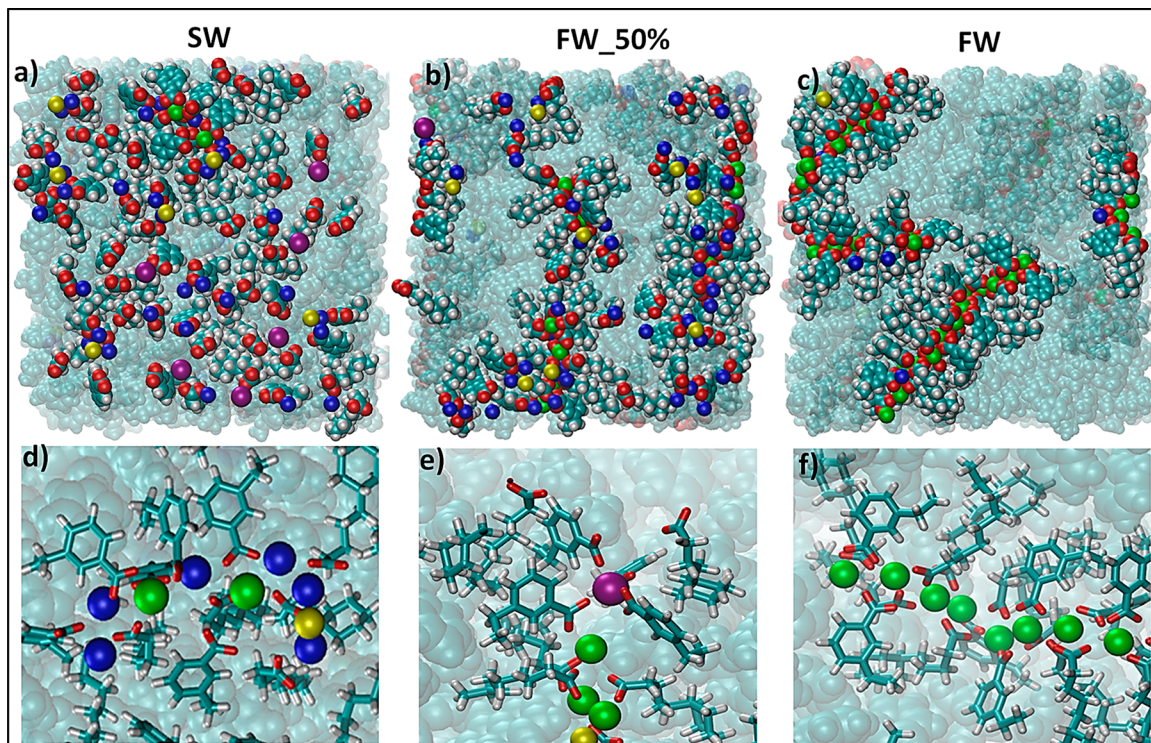


Figure 3. Oil–brine interface for seawater, formation water, and 50% diluted formation brine (a, b, and c). Panels e, d, and f are the cation's chelating patterns observed in our MD simulations. The nonpolar oil phase is shown in transparent cyan spheres. Metal cations are shown in colored spheres. Organic acids are shown as sticks. Color code: Ca²⁺, green; Mg²⁺, purple; Na⁺, blue; Cl⁻, yellow; O, red; C, cyan; H, white.

reason for the interface texture changes (Figure 3). The high concentration of Ca²⁺ in FW and its strong electrostatic interactions with the organic acids lead to forming a bilayer structure resulting in the salting-out effect. Thus, a depletion of the organic acids (surface-active molecules) occurs from the interface into the oil phase and leads to an increase in the IFT (Figure 3).⁴⁹ It is worth mentioning that in SW, the concentration of the divalent cations (Mg²⁺ (2110 ppm) and Ca²⁺ (650 ppm)) is much less than in FW (Mg²⁺ (2439 ppm) and Ca²⁺ (19 040 ppm)). Therefore, we did not see the formation of the bilayer structure with Mg²⁺ ions. Further, the dehydration-free energy of Mg²⁺ is the main hurdle for the formation of stable Mg²⁺-organic acid complexes.

3.3. Molecular Insights into the Oil–Brine Interface.

In order to further elucidate the oil–brine interface, we analyzed the simulated interfaces using the partial density, radial distribution function ($g(r)$), interaction energies (electrostatic and Van Der Waals (VDW)), hydrogen bonds (HB), and charge densities. The partial density along the normal to the interface indicates that the organic acids are highly impacted by the presence of the cations, particularly the divalent ones (Figure S6). The interface is getting thicker as the salinity increases. The interface thickness is 2.0, 2.82, and 2.92 nm for SW, FW_50%, and FW, respectively (here, we defined the interface thickness based on the organic acids' partial density, which is very close to the 90–90 scheme already reported,⁸¹ 90% of water and oil densities). Ca²⁺ ions cause the primary effect of salinity on the oil–brine IFT, which interacts strongly with organic acids. The Ca²⁺ density peak is aligned well with that of the organic acids, while Mg²⁺ is shifted inside the water phase (Figures S6 and S7). IFT increases with the concentration of Ca²⁺ ions, and a bilayer structure with the organic acids is observed. The bilayer encapsulates the metal

cations (Ca²⁺), which significantly attenuates the organic acid interaction with the water phase. In this scenario, the head groups of the organic acids are protected from water molecules via multidentate chelation patterns with the brine's cations (Figure 3).

The radial distribution function ($g(r)$) is an interesting analysis tool to extract detailed information about the liquid structure and detect short- and long-range packing. Herein, we used $g(r)$ to probe the interaction's probability between the carboxylate anion and the different cations in the brine (Figure 4); we found that the number density of the cations around the organic acids is more appropriate to monitor their interactions. Therefore, the $g(r)$ for the organic acids in Figure 4 is the counts of ions in each bin normalized by the bin's volume. However, we used the canonical $g(r)$ to monitor the packing of the organic acids, water–ions, organic acids–ions (individual brines; i.e., the $g(r)$ is normalized by the bin's volume and the bulk density). The $g(r)$ shown in Figure 4 shows that the organic acids display strong interactions with the different cations. As the salinity increases, the pattern of interactions changes, and it is a function of the type and cation concentration. On the one hand, the strength of the interactions between the organic acids with Na⁺ ions is getting weaker as we move from the SW to FW (Figure 4). On the other hand, the interaction with Ca²⁺ is getting stronger and follows the opposite trend of Na⁺. The interaction between the organic acid and Mg²⁺ is shifted to a shorter distance owing to its smaller ionic size than Na⁺ and Ca²⁺ ions (Figures 4 and S8). Therefore, its charge density is much higher than Na⁺ and Ca²⁺, which shortens the interaction distances with its chelating ligands. The interaction with Mg²⁺ does not follow the Ca²⁺-interaction profile due to the concentration difference between the two cations in SW and FW and the dehydration of

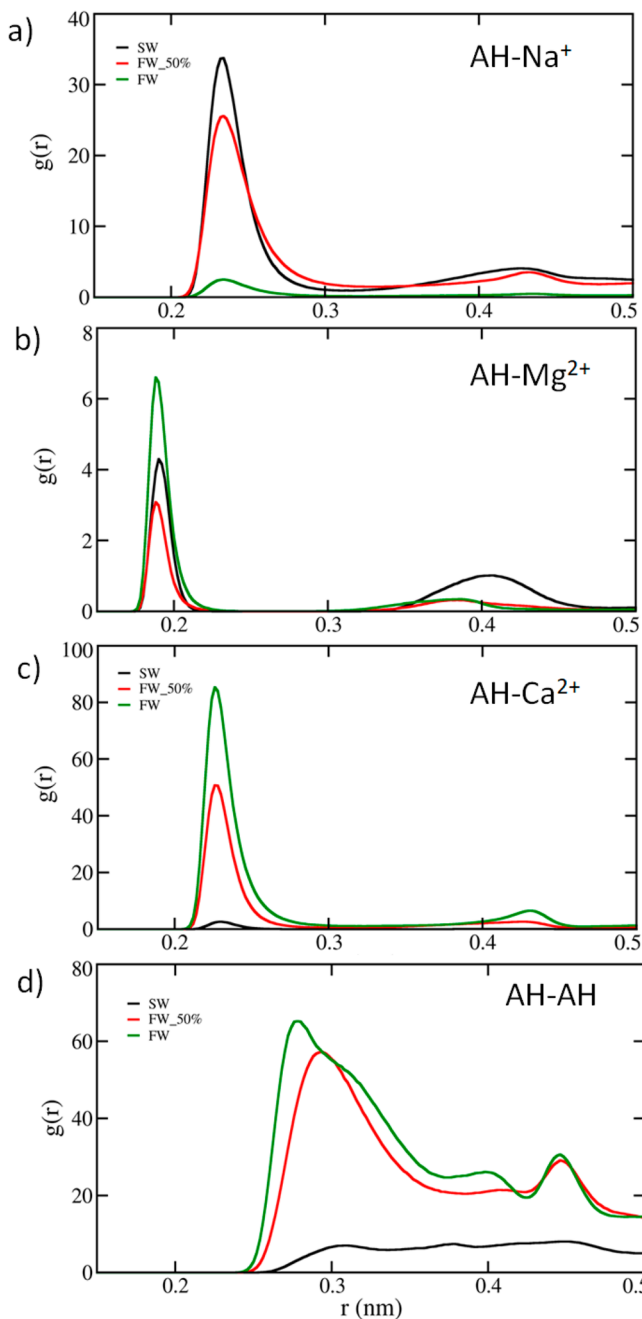


Figure 4. Radial distribution function ($g(r)$) calculated between the different cations and the headgroup (oxygen atoms) of the organic acids in different brine salinities (a–c). The ordering (packing) probability of the organic acids is also shown in panel d.

free energy. The concentration of Mg²⁺ in seawater is higher than in Ca²⁺ ions, and is noticeably lower than Na⁺. While in the connate (formation) water, Ca²⁺ is substantially higher than Mg²⁺. Ca²⁺ ions display the most potent interaction (the highest probability) with the organic acids. The change of IFT is well correlated with the concentration of Ca²⁺ ions. The packing of the organic acids at the interface is also salinity-dependent; the short-packing peak increases as the brine's salinity increases (Figure 4d), and it is also correlated with the Ca²⁺ concentration. Further, owing to the lower coordination number of Na⁺ compared to Ca²⁺; Na⁺ does not form large size aggregates with the organic acids mainly due to the electrostatic repulsion between the ligands (carboxylate

anion) in the first coordination shell. Therefore, the organic acids are distributed over the entire interface in the seawater. However, the larger size and the higher coordination number of Ca²⁺ lead to the formation of large aggregates with organic acids. The aggregation probability (i.e., the complexation degree between the organic acid and Ca²⁺) correlates well with the brine's salinity (Figure 4). The cation hydration (Figure S9) is also well associated with their interaction with the organic acids. Also, the increased salinity drops the hydration of the organic acids (Figure S10) and their interactions with Cl⁻ anions (Figure S11). The balance between the cation's dehydration free energies and the interaction free energies (mainly electrostatic) with the organic acids determines the final interaction shape between them. The dehydration-free energy of the Mg²⁺ ion is higher than that of Ca²⁺. Therefore, we observe a stronger interaction between the organic acids with Ca²⁺ than with Mg²⁺ ions. Compared with Na⁺, the high charge density of the divalent cations makes the organic acids prefer to bind the divalent over the monovalent cations. Chloride ions accumulate on the surface of organic acid–cation complexes in the second coordination shell (the first $g(r)$ peak of AH-Cl is located at 0.35 nm, while the AH-cation is at 0.25 nm for Ca²⁺ Na⁺, and 0.18 nm for Mg²⁺). The accumulation of Cl⁻ ions at both short (at 0.35 nm) and long range (at 0.5 nm) decrease as the salinity increases (Figure S11).

Regarding the hydrogen bond (HB) interactions between the aqueous and oil phases, we have calculated HB density (number/area) as the number of hydrogen bonds between oil–water and water–water molecules divided by the interfacial area. Increasing the brine's salinity from seawater to connate water significantly impacts HB density between oil–water and water–water (Figure S12). The presence of ions, especially the divalent ions, significantly perturbs the HB network at the interface and in the bulk of the aqueous phase. The ion–water interaction is also linked to the IFT–salinity relationship. The divalent (Ca²⁺ and Mg²⁺) ions have higher water coordination numbers than monovalent ions and, accordingly, disturb the HB network more at the interface. The charge density at the oil–brine interface highlighted an essential aspect of how the phases are interacting. Figure S13 shows that the charge density at the interface is +3 and -3.0 q/nm³ from the brine and oil sides, respectively. This demonstrates a strong polar interaction between the oil's polar components and the aqueous phase. In seawater, the concentration of Na⁺ at the interface is higher than its concentration in bulk. Water molecules are also in excess at the oil–seawater interface compared to the oil–FW_50% or the oil–FW interfaces. The accumulation of Ca²⁺ increases and replaces Na⁺ at the interface as the salinity increases from seawater to connate (formation) water. Chloride ions have much less charge density at the interface than monovalent and divalent cations and are mainly located in the bulk of the aqueous phase.

3.4. Revealing the Specificity and Synergy at the Oil–Brine Interface. The specificity of the molecular interactions at the oil–brine interface has been underlined through several MD simulations of the individual oil–brine interfaces, as detailed in the **Methodology** section. We performed a series of experiments covering a wide range of concentrations (0.1 mM to 5M; Figures 5 and S14 and Table S4). We also simulated the oil–brine interfaces using oil models M4, M5, and M6 (Figure 5). The oil models are different in the organic acid

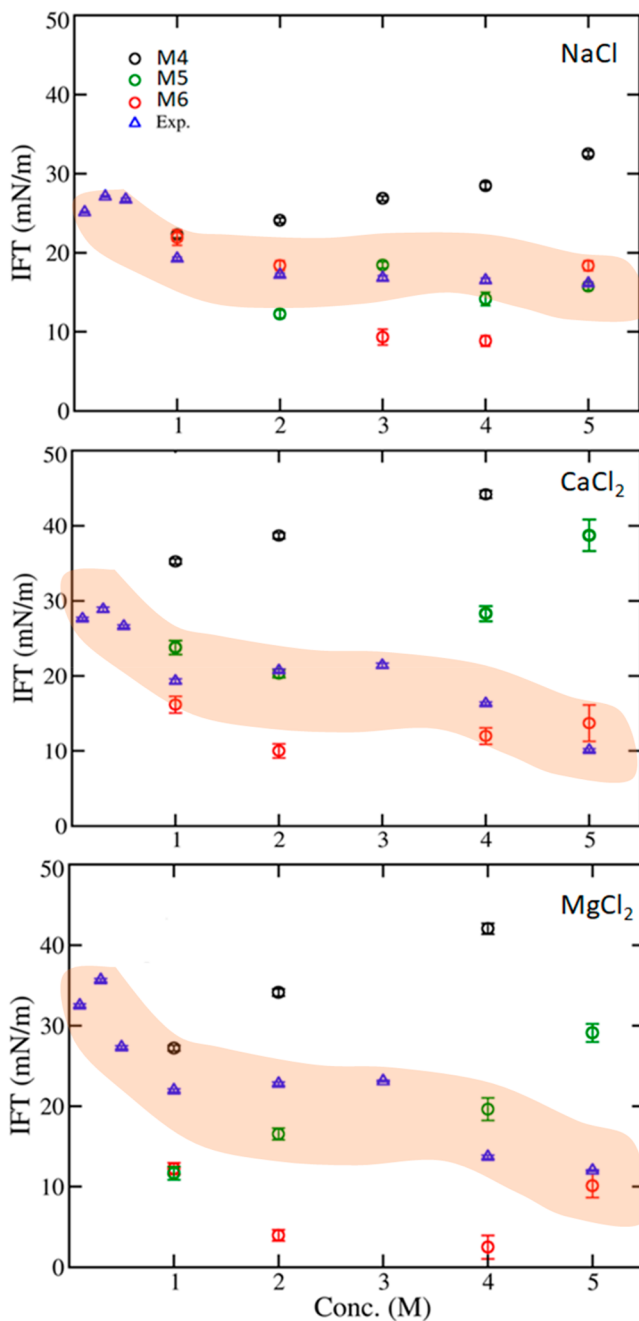


Figure 5. IFT of oil–brine systems as a function of the individual ion concentrations using different oil models (M4, M5, and M6) plotted with their experimental values.

content, and they have monolayer structural alignment over the interfacial area. For example, M6 has twice the organic acid concentration as M4. The study's objective is not to reproduce the experimental IFT values but to observe the experimental IFT trend by tuning the interface's saturation with the organic acids. The IFT of the oil–brine is dynamic and cannot be captured by only one model due to the slow deprotonation kinetics and thermodynamics of the organic acids. Moreover, we are using an empirical potential that does not include the system reactivity.

Experimentally, there is a peak of IFT as the brine salinity increases for all ions at low concentrations. The peak of IFT for MgCl_2 (5.8 mN/m) is higher than that of both CaCl_2 (3.3

mN/m) and NaCl (2.0 mN/m; Figures 5 and S14). The salting-in effect can explain the IFT trend in this range of salinity. Cations induce deprotonation of a small amount of the organic acids at such low concentrations via stabilizing their anionic form. The IFT peak might be correlated with the kinetics of the organic acid deprotonation. This behavior is well associated with the cation–water interactions. Mg^{2+} interacts strongly with water, and it does not induce much of the deprotonated organic acid. Indeed, the dehydration-free energy of Mg^{2+} is larger than that of either Ca^{2+} or Na^+ . Mg^{2+} displays an absolute increase of IFT (35.0 mN/m) with a higher value than that of NaCl (27.0 mN/m) and CaCl_2 (28.0 mN/m; Table S4).

IFT decreases as the ionic salt concentration increases and maintains its value from 1 to 5 M in the case of NaCl and reaches its minimum value at around 10.0 mN/m for the divalent (Ca^{2+}) system. Unfortunately, we cannot simulate such low concentrations considering the organic acids in their deprotonated state because the minimum ions needed to neutralize the deprotonated acids are already at 1 M concentration. At higher concentrations, we conducted long simulations for these interfaces (500 ns), which was necessary to ensure the convergence of the IFT. We observed uncertainties reaching up to 2.5 mN/m even at 500 ns, as in the case of CaCl_2 (Figure S15). In general, the IFT fluctuations in the case of divalent ions are higher than in the monovalent case, and it is a function of the organic acid concentration at the interface.

Figure 5 indicates that as the ionic salt concentration increases, the deprotonated organic acids diffuse into the interfacial area leading to IFT reduction. The results of M5 match the experimental IFT values well for NaCl except at 2 M. While using M4, the IFT response monotonically increases as the salt concentration increases because the deprotonated sites in M4 do not represent the experimental situation. We also observed an increase in the organic acids solubility at lower salt concentrations (1–3 M) into the aqueous phase due to the salting-in effect (as observed in the seawater brine). More organic acids diffused into the interface as the salt concentration increases. Focusing on NaCl brine, we observed the initiation of small crystallites of NaCl (SM) at the interface. The deprotonated acids served as a molecular platform for the NaCl crystal growth, which explains why IFT remains constant though the salt concentrations increase (Figures 5 and S16). Further analysis is found in the SI (S17).

In the case of divalent cations, IFT exhibits a plateau region in the salinity range 1 to 3 M then monotonically decreases, reaching its minimum value at 5 M (Figure 5). There is a good agreement between the calculated and the experimental IFT values using the M6 oil model at high concentrations (5 M) and using the M5 oil model at lower concentrations (2 M). At higher concentrations, more deprotonated acids are required to fit the experimental IFT values. As the salt concentration increases, more organic acids diffuse into the interface and lead to IFT reduction (Figure 5). Higher salt concentrations exhibit a higher coverage of the organic acids at the oil–brine interface than at a lower concentration (Figure 6). The interfacial texture shown in Figure 6 (b for 2 M and c for 5 M concentrations) demonstrates the concentration effect on the coverage area by the organic acids. Such accumulation is evident from the mass and charge densities plots (Figures S21 and S22). The same trend is observed for MgCl_2 (Figures S23 and S24). The increased interfacial coverage of the organic

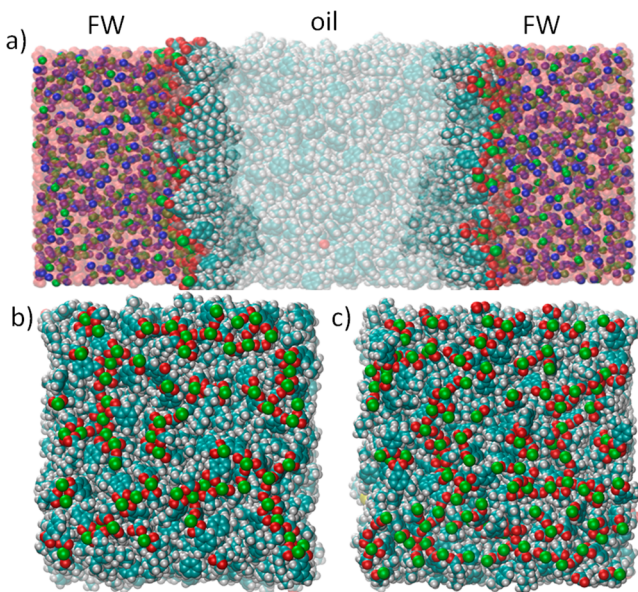


Figure 6. Oil–brine interface for CaCl_2 system. (a) Oil–brine (FW) interface along the z axis at 5 M concentration. The interfacial area (i.e., xy plane) is shown at 2 M (b) and 5 M (c) concentrations. The molecular models are shown in spheres. Water molecules are shown in transparent red spheres. Color code: H, white; O, red; C, cyan; Cl^- , blue; Ca^{2+} , green. Crude oil simulated using M5 at 2 M concentrations and M6 at 5 M concentrations.

acids is the main reason for the IFT reduction. Also, at higher salt concentrations, the lack of water induces the formation of small aggregates of CaCl_2 or MgCl_2 (Figures S25 and S26). Radial distribution function $g(r)$ indicates that the probability of the metal–acid interactions is higher than between metals with either water or Cl^- ions. In the case of CaCl_2 , the tendency to form small aggregates is higher than MgCl_2 brine, despite the concentration of the organic acids being the same for both salts at 5 M (M6 oil model). The hydration-free energy difference between the two cations favors the higher aggregation tendency for CaCl_2 versus MgCl_2 .

An important question that one should attempt to answer here is, *Why did we not observe the bilayer structure of the organic acids and the complete encapsulation of the cations in the individual oil–brine interfaces (even at high concentrations), as in the formation brine complex?* To answer this question, we need to go deeper into the molecular interactions at these interfaces. We analyzed the different interactions at the oil–brine interfaces (Figure S27). The metal–acid interactions are more substantial in individual brines than in either seawater or formation water. Nevertheless, we do not observe the cation's encapsulation. The hydration of the organic acids seems irrelevant to explain the IFT increase in SW and FW. The metal–water and metal– Cl^- interactions are more significant than the metal–acid interactions in the individual brines. However, in the case of formation water, the metal–acid interaction is more considerable than the metal–water interactions and is close to the metal– Cl^- interaction. Also, the calcium contribution to the total metal–acid in formation water is significantly dominant (Figure S28). At the same time, the Na^+ ion contribution to the total metal– Cl^- interactions is the dominant one (Figure S29) in the formation water. Therefore, we observe metal encapsulation in FW and not in the individual brines. The specificity between Ca^{2+} and organic acids and the synergy between Na^+ and Ca^{2+} explain well the

experimental IFT increase in the high salinity mixed brine (formation water) and the IFT reduction in the case of the individual brines. Such specificity of Ca^{2+} ions for the organic acids at the oil–brine interface is already reported.⁸² Altogether, the interplay between the electrostatic interactions around the cations and its dehydration-free energies is the main parameter that controls the ionic specificity and synergy, affecting the oil–brine interfacial properties. Without considering the complex composition of both the brine and crude oil, we could not explain the experimental IFT of the crude oil–brine system.

4. CONCLUSION

A thorough investigation of the brine–oil interface has been performed using MD simulations and the pendant drop method. The study brings new atomic-scale insights into the interface intrinsic interactions and structures. The specificity of the organic acid– Ca^{2+} has been revealed using MD simulation. A synergy effect between the various ions in the high salinity mixed brine has been observed. The specificity and synergy effects are underlined by a confrontation of the results of the mixed and individual brine–oil interfaces. On the one hand, in the simulation of crude oil without the organic acids, we observed an increase of IFT as the salinity increases (Figures S30 and S31).^{31,32} On the other hand, the simulation of the oil–brine at low salt concentrations using crude oil including organic acids showed a reduction of the IFT (Figure 1b). Further reduction in the IFT has been observed at 5 M of the oil–individual brines. However, interestingly, when we combined the structural complexity of the oil and brine, we observed an increase of the IFT with the salinity in the case of sea, and formation water, in agreement with the experimental results.

The interaction preference of the organic acids toward Ca^{2+} (rather than Na^+ or Mg^{2+}) and other molecular interactions (metal–water and metal– Cl^-) are the origin of the negative salinity effect on the IFT in the case of the mixed brine (formation water). Indeed, the strong interactions between Na^+ with water and Cl^- as well as the preference of Ca^{2+} to bind carboxylate leads to bilayer structures between the Ca^{2+} and organic acids that deplete them at the oil–brine interface, and thus the IFT increases. However, unlike the real oil–brine system, the metal–water and the metal– Cl^- interactions in the individual brine neutralize the metal–organic acid interaction, leading to the absence of any metal encapsulation. Overall, the perturbation of the water structure at the interface, dehydration-free energies, and the metal– Cl^- and metal–organic acid interaction types shape the IFT–salinity relationship.

Our study emphasizes the importance of considering the complex composition of both brine and crude oil to describe the brine–oil interface accurately. It paves the way for better optimizing cEOR formulations and understanding the low salinity oil recovery processes.

Finally, despite the thorough and rigorous approach presented herein, more investigations are required to fully understand the brine–oil interface. For example, reactive MD simulations are necessary to understand the organic acid deprotonation's kinetics and thermodynamics.

ASSOCIATED CONTENT

Supporting Information

The Supporting Information is available free of charge at <https://pubs.acs.org/doi/10.1021/acs.energyfuels.1c02133>.

Experimental compositional analysis of the crude oil "SARA", details of the MD models of the crude oil components, partial density, RDFs, hydrogen bond analysis, partial charge densities, energetic analysis, the experimental IFT of the individual oil–brines for the 10 considered concentrations, IFT of the brine–oil in the absence of organic acids ([PDF](#))

AUTHOR INFORMATION

Corresponding Author

Safwat Abdel-Azeim – Center for Integrative Petroleum Research (CIPR), College of Petroleum Engineering and Geosciences, King Fahd University of Petroleum and Minerals (KFUPM), Dhahran 31261, Saudi Arabia; [orcid.org/0000-0001-8611-1251](#); Email: abdelazeim@kfupm.edu.sa

Authors

Sivabalan Sakthivel – Center for Integrative Petroleum Research (CIPR), College of Petroleum Engineering and Geosciences, King Fahd University of Petroleum and Minerals (KFUPM), Dhahran 31261, Saudi Arabia; [orcid.org/0000-0002-0738-2895](#)

Tarek A. Kandiel – Department of Chemistry, King Fahd University of Petroleum and Minerals (KFUPM), Dhahran 31261, Saudi Arabia

Mazen Y. Kanj – Center for Integrative Petroleum Research (CIPR), College of Petroleum Engineering and Geosciences, King Fahd University of Petroleum and Minerals (KFUPM), Dhahran 31261, Saudi Arabia; [orcid.org/0000-0002-2674-4505](#)

Complete contact information is available at:
<https://pubs.acs.org/10.1021/acs.energyfuels.1c02133>

Notes

The authors declare no competing financial interest.

ACKNOWLEDGMENTS

The authors acknowledge the support of the KAUST Supercomputer Lab in Thuwal, Saudi Arabia, for permission to use its computational resources and Alfahd supercomputer of the college of petroleum engineering and geosciences (CPG).

REFERENCES

- (1) Bera, A.; Mandal, A.; Guha, B. B. Synergistic Effect of Surfactant and Salt Mixture on Interfacial Tension Reduction between Crude Oil and Water in Enhanced Oil Recovery. *J. Chem. Eng. Data* **2014**, *59* (1), 89–96.
- (2) Georgiadis, A.; Maitland, G.; Trusler, J. M.; Bismarck, A. Interfacial Tension Measurements of the (H₂O+ n-Decane+ CO₂) Ternary System at Elevated Pressures and Temperatures. *J. Chem. Eng. Data* **2011**, *56* (12), 4900–4908.
- (3) Escrochi, M.; Mehranbod, N.; Ayatollahi, S. The Gas–Oil Interfacial Behavior during Gas Injection into an Asphaltenic Oil Reservoir. *J. Chem. Eng. Data* **2013**, *58* (9), 2513–2526.
- (4) Wen, B.; Sun, C.; Bai, B.; Gatapova, E. Y.; Kabov, O. A. Ionic Hydration-Induced Evolution of Decane–Water Interfacial Tension. *Phys. Chem. Chem. Phys.* **2017**, *19* (22), 14606–14614.

(5) Buckley, J. S.; Fan, T. Crude Oil/Brine Interfacial Tensions1. *Petrophysics* **2007**, *48* (03), SPWLA-2007-v48n3a1.

(6) Sztukowski, D. M.; Yarranton, H. W. Characterization and Interfacial Behavior of Oil Sands Solids Implicated in Emulsion Stability. *J. Dispersion Sci. Technol.* **2004**, *25* (3), 299–310.

(7) Marshall, A. G.; Rodgers, R. P. Petroleomics: The next Grand Challenge for Chemical Analysis. *Acc. Chem. Res.* **2004**, *37* (1), 53–59.

(8) Bayona, J. M.; Domínguez, C.; Albaiges, J. Analytical Developments for Oil Spill Fingerprinting. *Trends Environ. Anal. Chem.* **2015**, *5*, 26–34.

(9) Sandrea, I.; Sandrea, R. Global Oil Reserves-1: Recovery Factors Leave Vast Target for EOR Technologies. *Oil Gas J.* **2007**, *105* (41), 44.

(10) Siggel, L.; Santa, M.; Hansch, M.; Nowak, M.; Ranft, M.; Weiss, H.; Hajnal, D.; Schreiner, E.; Oetter, G.; Tinsley, J. A New Class of Viscoelastic Surfactants for Enhanced Oil Recovery. *Proceedings of the SPE Improved Oil Recovery Symposium*; Society of Petroleum Engineers: Tulsa, OK, April 14–18, 2012; DOI: [10.2118/153969-MS](https://doi.org/10.2118/153969-MS).

(11) Morvan, M.; Moreau, P.; Degre, G.; Leng, J.; Masselon, C.; Bouillot, J.; Zaitoun, A. New Viscoelastic Fluid for Chemical EOR. *Proceedings of the SPE International Symposium on Oilfield Chemistry*; Society of Petroleum Engineers: The Woodlands, TX, April 20–22, 2009; DOI: [10.2118/121675-MS](https://doi.org/10.2118/121675-MS).

(12) Thomas, S. Enhanced Oil Recovery an Overview. *Oil Gas Sci. Technol.* **2008**, *63* (1), 9–19.

(13) Wei, B.; Romero-Zérón, L.; Rodrigue, D. Oil Displacement Mechanisms of Viscoelastic Polymers in Enhanced Oil Recovery (EOR): A Review. *J. Pet. Explor. Prod. Technol.* **2014**, *4* (2), 113–121.

(14) Hirasaki, G. J.; Miller, C. A.; Puerto, M. Recent Advances in Surfactant EOR. *SPE J.* **2011**, *16* (04), 889–907.

(15) Kamal, M. S.; Hussein, I. A.; Sultan, A. S. Review on Surfactant Flooding: Phase Behavior, Retention, IFT, and Field Applications. *Energy Fuels* **2017**, *31* (8), 7701–7720.

(16) Standnes, D. C.; Skjevrak, I. Literature Review of Implemented Polymer Field Projects. *J. Pet. Sci. Eng.* **2014**, *122*, 761–775.

(17) Al Hashmi, A. R.; Al Maamari, R. S.; Al Shabibi, I. S.; Mansoor, A. M.; Zaitoun, A.; Al Sharji, H. H. Rheology and Mechanical Degradation of High-Molecular-Weight Partially Hydrolyzed Polyacrylamide during Flow through Capillaries. *J. Pet. Sci. Eng.* **2013**, *105*, 100–106.

(18) Al-Dhafeeri, A. M.; Nasr-El-Din, H. A.; Seright, R. S.; Sydansk, R. D. High-Permeability Carbonate Zones (Super-k) in Ghawar Field (Saudi Arabia): Identified, Characterized, and Evaluated for Gel Treatments. *Proceedings of the SPE International Improved Oil Recovery Conference in Asia Pacific*; Society of Petroleum Engineers: Kuala Lumpur, Malaysia, December 5–6, 2005; DOI: [10.2118/97542-MS](https://doi.org/10.2118/97542-MS).

(19) Rosen, M. J.; Wang, H.; Shen, P.; Zhu, Y. Ultralow Interfacial Tension for Enhanced Oil Recovery at Very Low Surfactant Concentrations. *Langmuir* **2005**, *21* (9), 3749–3756.

(20) Barati-Harooni, A.; Soleymanzadeh, A.; Tatar, A.; Najafi-Marghamaleki, A.; Samadi, S.-J.; Yari, A.; Roushani, B.; Mohammadi, A. H. Experimental and Modeling Studies on the Effects of Temperature, Pressure and Brine Salinity on Interfacial Tension in Live Oil–Brine Systems. *J. Mol. Liq.* **2016**, *219*, 985–993.

(21) Kumar, S.; Mandal, A. Studies on Interfacial Behavior and Wettability Change Phenomena by Ionic and Nonionic Surfactants in Presence of Alkalies and Salt for Enhanced Oil Recovery. *Appl. Surf. Sci.* **2016**, *372*, 42–51.

(22) Aveyard, R.; Haydon, D. A. Thermodynamic Properties of Aliphatic Hydrocarbon/Water Interfaces. *Trans. Faraday Soc.* **1965**, *61*, 2255–2261.

(23) Jennings, H. Y., Jr. The Effect of Temperature and Pressure on the Interfacial Tension of Benzene–Water and Normal Decane–Water. *J. Colloid Interface Sci.* **1967**, *24* (3), 323–329.

(24) Rehfeld, S. J. Adsorption of Sodium Dodecyl Sulfate at Various Hydrocarbon–Water Interfaces. *J. Phys. Chem.* **1967**, *71* (3), 738–745.

- (25) Hjelmeland, O. S.; Larrondo, L. E. Experimental Investigation of the Effects of Temperature, Pressure, and Crude Oil Composition on Interfacial Properties. *SPE Reservoir Eng.* **1986**, *1* (04), 321–328.
- (26) Goebel, A.; Lunkenheimer, K. Interfacial Tension of the Water/n-Alkane Interface. *Langmuir* **1997**, *13* (2), 369–372.
- (27) Van Buuren, A. R.; Marrink, S. J.; Berendsen, H. J. A Molecular Dynamics Study of the Decane/Water Interface. *J. Phys. Chem.* **1993**, *97* (36), 9206–9212.
- (28) Patel, H. A.; Nauman, E. B.; Garde, S. Molecular Structure and Hydrophobic Solvation Thermodynamics at an Octane–Water Interface. *J. Chem. Phys.* **2003**, *119* (17), 9199–9206.
- (29) Beattie, J. K.; Djerdjev, A. M. The Pristine Oil/Water Interface: Surfactant-Free Hydroxide-Charged Emulsions. *Angew. Chem., Int. Ed.* **2004**, *43* (27), 3568–3571.
- (30) Kereszturi, Á.; Jedlovszky, P. Computer Simulation Investigation of the Water–Benzene Interface in a Broad Range of Thermodynamic States from Ambient to Supercritical Conditions. *J. Phys. Chem. B* **2005**, *109* (35), 16782–16793.
- (31) Shi, K.; Lian, C.; Bai, Z.; Zhao, S.; Liu, H. Dissipative Particle Dynamics Study of the Water/Benzene/Caprolactam System in the Absence or Presence of Non-Ionic Surfactants. *Chem. Eng. Sci.* **2015**, *122*, 185–196.
- (32) Cai, B.-Y.; Yang, J.-T.; Guo, T.-M. Interfacial Tension of Hydrocarbon+ Water/Brine Systems under High Pressure. *J. Chem. Eng. Data* **1996**, *41* (3), 493–496.
- (33) Vijapurapu, C. S.; Rao, D. N. Compositional Effects of Fluids on Spreading, Adhesion and Wettability in Porous Media. *Colloids Surf, A* **2004**, *241* (1–3), 335–342.
- (34) Moeini, F.; Hemmati-Sarapardeh, A.; Ghazanfari, M.-H.; Masihi, M.; Ayatollahi, S. Toward Mechanistic Understanding of Heavy Crude Oil/Brine Interfacial Tension: The Roles of Salinity, Temperature and Pressure. *Fluid Phase Equilib.* **2014**, *375*, 191–200.
- (35) Abdel-Wali, A. A. Effect of Simple Polar Compounds and Salinity on Interfacial Tension and Wettability of Rock/Oil/Brine System. *J. King Saud Univ., Eng. Sci.* **1996**, *8* (2), 153–162.
- (36) Alotaibi, M. B.; Nasr-El-Din, H. A. Salinity of Injection Water and Its Impact on Oil Recovery. *Proceedings of the international EUROPEC/EAGE conference and exhibition*; Society of Petroleum Engineers: Amsterdam, The Netherlands, June 8–11, 2009; DOI: [10.2118/121569-MS](https://doi.org/10.2118/121569-MS).
- (37) Serrano-Saldaña, E.; Domínguez-Ortiz, A.; Pérez-Aguilar, H.; Kornhauser-Strauss, I.; Rojas-González, F. Wettability of Solid/Brine/n-Dodecane Systems: Experimental Study of the Effects of Ionic Strength and Surfactant Concentration. *Colloids Surf, A* **2004**, *241* (1–3), 343–349.
- (38) Bai, J.-M.; Fan, W.-Y.; Nan, G.-Z.; Li, S.-P.; Yu, B.-S. Influence of Interaction between Heavy Oil Components and Petroleum Sulfonate on the Oil–Water Interfacial Tension. *J. Dispersion Sci. Technol.* **2010**, *31* (4), 551–556.
- (39) Sayed, A. M.; Olesen, K. B.; Alkahala, A. S.; Sølling, T. I.; Alyafei, N. The Effect of Organic Acids and Salinity on the Interfacial Tension of N-Decane/Water Systems. *J. Pet. Sci. Eng.* **2019**, *173*, 1047–1052.
- (40) Li, W.; Nan, Y.; Wen, X.; Wang, W.; Jin, Z. Effects of Salinity and N-, S-, and O-Bearing Polar Components on Light Oil–Brine Interfacial Properties from Molecular Perspectives. *J. Phys. Chem. C* **2019**, *123* (38), 23520–23528.
- (41) Zhao, J.; Yao, G.; Ramisetti, S. B.; Hammond, R. B.; Wen, D. Molecular Dynamics Simulation of the Salinity Effect on the N-Decane/Water/Vapor Interfacial Equilibrium. *Energy Fuels* **2018**, *32* (11), 11080–11092.
- (42) Tang, G. Q.; Morrow, N. R. Salinity, Temperature, Oil Composition, and Oil Recovery by Waterflooding. *SPE Reservoir Eng.* **1997**, *12* (04), 269–276.
- (43) Panda, S. K.; Andersson, J. T.; Schrader, W. Characterization of Supercomplex Crude Oil Mixtures: What Is Really in There? *Angew. Chem., Int. Ed.* **2009**, *48* (10), 1788–1791.
- (44) Sedghi, M.; Piri, M.; Goual, L. Atomistic Molecular Dynamics Simulations of Crude Oil/Brine Displacement in Calcite Mesopores. *Langmuir* **2016**, *32* (14), 3375–3384.
- (45) Sørbo, I. G. *Polar Components in Crude Oils and Their Correlation to Physiochemical Properties*; University of Bergen, 2016.
- (46) Yi, C.; Xie, S.; Qiu, X. Salting-out Effect of Dipotassium Hydrogen Phosphate on the Recovery of Acetone, Butanol, and Ethanol from a Prefractionator. *J. Chem. Eng. Data* **2014**, *59* (5), 1507–1514.
- (47) Armenante, P. M.; Karlsson, H. T. Salting-out Parameters for Organic Acids. *J. Chem. Eng. Data* **1982**, *27* (2), 155–156.
- (48) Standal, S. H.; Blokhus, A. M.; Haavik, J.; Skauge, A.; Barth, T. Partition Coefficients and Interfacial Activity for Polar Components in Oil/Water Model Systems. *J. Colloid Interface Sci.* **1999**, *212* (1), 33–41.
- (49) Lashkarbolooki, M.; Ayatollahi, S.; Riazi, M. The Impacts of Aqueous Ions on Interfacial Tension and Wettability of an Asphaltenic–Acidic Crude Oil Reservoir during Smart Water Injection. *J. Chem. Eng. Data* **2014**, *59* (11), 3624–3634.
- (50) Kirch, A.; Celaschi, Y. M.; de Almeida, J. M.; Miranda, C. R. Brine–Oil Interfacial Tension Modeling: Assessment of Machine Learning Techniques Combined with Molecular Dynamics. *ACS Appl. Mater. Interfaces* **2020**, *12* (13), 15837–15843.
- (51) Drelich, J.; Fang, C.; White, C. L. Measurement of Interfacial Tension in Fluid–Fluid Systems. *Encycl. Surf. Colloid Sci.* **2002**, *3*, 3158–3163.
- (52) Andreas, J. M.; Hauser, E. A.; Tucker, W. B. Boundary Tension by Pendant Drops. *J. Phys. Chem.* **1938**, *42* (8), 1001–1019.
- (53) Stauffer, C. E. The Measurement of Surface Tension by the Pendant Drop Technique. *J. Phys. Chem.* **1965**, *69* (6), 1933–1938.
- (54) Mahajan, S.; Konar, S. K.; Boocock, D. G. b. Determining the Acid Number of Biodiesel. *J. Am. Oil Chem. Soc.* **2006**, *83* (6), 567–570.
- (55) Zafar, F.; Mandal, P. C.; Shaari, K. Z. b. K.; Moniruzzaman, M. Total Acid Number Reduction of Naphthenic Acid Using Subcritical Methanol and 1-Butyl-3-Methylimidazolium Octylsulfate. *Procedia Eng.* **2016**, *148*, 1074–1080.
- (56) Trejo, F.; Centeno, G.; Ancheyta, J. Precipitation, Fractionation and Characterization of Asphaltenes from Heavy and Light Crude Oils. *Fuel* **2004**, *83* (16), 2169–2175.
- (57) Alonso-Ramírez, G.; Cuevas-García, R.; Sánchez-Minero, F.; Ramírez, J.; Moreno-Montiel, M.; Silva-Oliver, G.; Ancheyta, J.; Carballo-Vielman, R. Catalytic Hydrocracking of a Mexican Heavy Oil on a MoS₂/Al₂O₃catalyst: II. Study of the Transformation of Isolated Aromatics Fraction Obtained from SARA Analysis. *Fuel* **2021**, *288*, 119541.
- (58) Hess, B.; Kutzner, C.; Van Der Spoel, D.; Lindahl, E. GROMACS 4: Algorithms for Highly Efficient, Load-Balanced, and Scalable Molecular Simulation. *J. Chem. Theory Comput.* **2008**, *4* (3), 435–447.
- (59) Jorgensen, W. L.; Tirado-Rives, J. The OPLS [Optimized Potentials for Liquid Simulations] Potential Functions for Proteins, Energy Minimizations for Crystals of Cyclic Peptides and Crambin. *J. Am. Chem. Soc.* **1988**, *110* (6), 1657–1666.
- (60) Jorgensen, W. L.; Maxwell, D. S.; Tirado-Rives, J. Development and Testing of the OPLS All-Atom Force Field on Conformational Energies and Properties of Organic Liquids. *J. Am. Chem. Soc.* **1996**, *118* (45), 11225–11236.
- (61) Berendsen, H. J. C.; Grigera, J. R.; Straatsma, T. P. The Missing Term in Effective Pair Potentials. *J. Phys. Chem.* **1987**, *91* (24), 6269–6271.
- (62) Abdel-Azeim, S.; Kanj, M. Y. Dynamics, Aggregation, and Interfacial Properties of the Partially Hydrolyzed Polyacrylamide Polymer for Enhanced Oil Recovery Applications: Insights from Molecular Dynamics Simulations. *Energy Fuels* **2018**, *32* (3), 3335–3343.
- (63) Boçan, V.; Ustach, V.; Faller, R.; Leonhard, K. Direct Phase Equilibrium Simulations of NIPAM Oligomers in Water. *J. Phys. Chem. B* **2016**, *120* (13), 3434–3440.

- (64) Mafi, A.; Hu, D.; Chou, K. C. Complex Formations between Surfactants and Polyelectrolytes of the Same Charge on a Water Surface. *Langmuir* **2017**, *33* (32), 7940–7946.
- (65) Alade, O. S.; Abdel-Azeim, S.; Mahmoud, M.; Hamdy, M.; Al-Shehri, D. A.; Mokheimer, E. Studies of Interaction between Bitumen and Thermochemical Fluid (TCF): Insights from Experiment and Molecular Dynamics Simulations. *Appl. Surf. Sci.* **2020**, *S27*, 146942.
- (66) Darden, T.; York, D.; Pedersen, L. Particle Mesh Ewald: An N-Log (N) Method for Ewald Sums in Large Systems. *J. Chem. Phys.* **1993**, *98* (12), 10089–10092.
- (67) Hess, B.; Bekker, H.; Berendsen, H. J.; Fraaije, J. G. LINCS: A Linear Constraint Solver for Molecular Simulations. *J. Comput. Chem.* **1997**, *18* (12), 1463–1472.
- (68) Nosé, S. A Unified Formulation of the Constant Temperature Molecular Dynamics Methods. *J. Chem. Phys.* **1984**, *81* (1), 511–519.
- (69) Hoover, W. G. Canonical Dynamics: Equilibrium Phase-Space Distributions. *Phys. Rev. A: At., Mol., Opt. Phys.* **1985**, *31* (3), 1695.
- (70) Martonák, R.; Laio, A.; Parrinello, M. Predicting Crystal Structures: The Parrinello-Rahman Method Revisited. *Phys. Rev. Lett.* **2003**, *90* (7), No. 075503.
- (71) Kunieda, M.; Nakaoka, K.; Liang, Y.; Miranda, C. R.; Ueda, A.; Takahashi, S.; Okabe, H.; Matsuoka, T. Self-Accumulation of Aromatics at the Oil-Water Interface through Weak Hydrogen Bonding. *J. Am. Chem. Soc.* **2010**, *132* (51), 18281–18286.
- (72) Jian, C.; Poopari, M. R.; Liu, Q.; Zerpa, N.; Zeng, H.; Tang, T. Reduction of Water/Oil Interfacial Tension by Model Asphaltenes: The Governing Role of Surface Concentration. *J. Phys. Chem. B* **2016**, *120* (25), 5646–5654.
- (73) Mikami, Y.; Liang, Y.; Matsuoka, T.; Boek, E. S. Molecular Dynamics Simulations of Asphaltenes at the Oil-Water Interface: From Nanoaggregation to Thin-Film Formation. *Energy Fuels* **2013**, *27* (4), 1838–1845.
- (74) Mahmoud, M. A.; Abdalgawad, K. Z. Chelating-Agent Enhanced Oil Recovery for Sandstone and Carbonate Reservoirs. *SPE J.* **2015**, *20* (03), 483–495.
- (75) Aqvist, J. Ion-Water Interaction Potentials Derived from Free Energy Perturbation Simulations. *J. Phys. Chem.* **1990**, *94* (21), 8021–8024.
- (76) Chandrasekhar, J.; Spellmeyer, D. C.; Jorgensen, W. L. Energy Component Analysis for Dilute Aqueous Solutions of Lithium (1+), Sodium (1+), Fluoride (1-), and Chloride (1-) Ions. *J. Am. Chem. Soc.* **1984**, *106* (4), 903–910.
- (77) Rivera-Barrera, D.; Rueda-Chacón, H.; Molina, D., V Prediction of the Total Acid Number (TAN) of Colombian Crude Oils via ATR-FTIR Spectroscopy and Chemometric Methods. *Talanta* **2020**, *206*, 120186.
- (78) Alabi, O. O.; Bowden, S. A.; Parnell, J. Simultaneous and Rapid Asphaltene and TAN Determination for Heavy Petroleum Using an H-Cell. *Anal. Methods* **2014**, *6* (11), 3651–3660.
- (79) Havre, T. E.; Sjöblom, J.; Vindstad, J. E. Oil/Water-Partitioning and Interfacial Behavior of Naphthenic Acids. *J. Dispersion Sci. Technol.* **2003**, *24* (6), 789–801.
- (80) Acevedo, S.; Gutierrez, X.; Rivas, H. Bitumen-in-Water Emulsions Stabilized with Natural Surfactants. *J. Colloid Interface Sci.* **2001**, *242* (1), 230–238.
- (81) Jang, S. S.; Lin, S.-T.; Maiti, P. K.; Blanco, M.; Goddard, W. A.; Shuler, P.; Tang, Y. Molecular Dynamics Study of a Surfactant-Mediated Decane-Water Interface: Effect of Molecular Architecture of Alkyl Benzene Sulfonate. *J. Phys. Chem. B* **2004**, *108* (32), 12130–12140.
- (82) Taylor, S. E.; Chu, H. T. Metal Ion Interactions with Crude Oil Components: Specificity of Ca²⁺ Binding to Naphthenic Acid at an Oil/Water Interface. *Colloids Interfaces* **2018**, *2* (3), 40.